







RESEARCH ARTICLE | OCTOBER 01 2024

Development of a compact bolometer camera concept for investigation of radiation asymmetries at Wendelstein 7-X

G. Partesotti ; F. Reimold ; J. Ruhnau; A. Tsikouras ; D. Kubeneck ; D. Zhang ; P. Geißler ; W7-X Team



Rev. Sci. Instrum. 95, 103503 (2024)

<https://doi.org/10.1063/5.0207762>



View
Online



Export
Citation

Articles You May Be Interested In

Diagnostics design for steady-state operation of the Wendelstein 7-X stellarator

Rev. Sci. Instrum. (October 2010)

A divertor scraper observation system for the Wendelstein 7-X stellarator

Rev. Sci. Instrum. (August 2018)

Performance of new crystal cathode pressure gauges for long-pulse operation in the Wendelstein 7-X stellarator

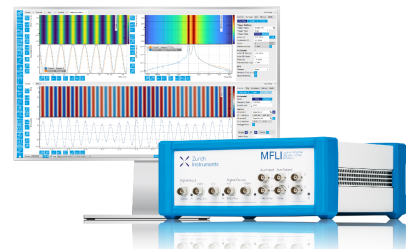
Rev. Sci. Instrum. (December 2019)

Challenge us.

What are your needs for periodic signal detection?



Find out more



Development of a compact bolometer camera concept for investigation of radiation asymmetries at Wendelstein 7-X

Cite as: Rev. Sci. Instrum. 95, 103503 (2024); doi: 10.1063/5.0207762
Submitted: 11 March 2024 • Accepted: 13 September 2024 •
Published Online: 1 October 2024



G. Partesotti,^{a)}  F. Reimold,  J. Ruhnau, A. Tsikouras,  D. Kubeneck,  D. Zhang,  P. Geißler, 
and W7-X Team^{b)}

AFFILIATIONS

Max-Planck-Institut für Plasmaphysik, Greifswald, Germany

^{a)} Author to whom correspondence should be addressed: gabriele.partesotti@ipp.mpg.de

^{b)} See the authors list in O. Grulke *et al.*, Nucl. Fusion **64**, 112002 (2024).

ABSTRACT

Power exhaust is one of the central challenges in magnetically confined fusion plasmas. Radiative detachment can be employed to reduce particle and heat fluxes to the divertor target, mitigating divertor damage and erosion. However, accomplishing this for a non-axisymmetric machine such as Wendelstein 7-X is a non-trivial task because of the complex role of transport and plasma-wall interaction in a three-dimensional magnetic field topology. We introduce a new bolometer camera design that can be easily installed in multiple toroidal locations and adapted to the required geometry, providing additional spatial coverage. This can be used to locally enhance tomographic capabilities or to resolve spatial variations of the plasma emissivity. By including these non-uniformities in the total radiated power estimate, global power balance measurements can be improved. We model each bolometer camera using ray tracing. We then analyze the forward-modeled detector response to several physically motivated synthetic emission phantoms with respect to its capability to quantify the local average emissivity. The results prove this concept as a promising asset for the investigation of poloidal and toroidal radiated power asymmetries in Wendelstein 7-X. The first CBC prototypes have undergone development and installation for the next experimental campaign.

© 2024 Author(s). All article content, except where otherwise noted, is licensed under a Creative Commons Attribution (CC BY) license (<http://creativecommons.org/licenses/by/4.0/>). <https://doi.org/10.1063/5.0207762>

I. INTRODUCTION

When compared to tokamaks, stellarator reactors promise a more stable, steady-state plasma operation, which is ideal for applications in a fusion power plant. On the other hand, this increased reliability requires a more complicated, three-dimensional magnetic field topology. This makes stellarators more challenging to design and study when compared to the axially symmetric tokamaks.¹

The Wendelstein 7-X (W7-X) magnetic field geometry presents a five-fold stellarator symmetry, meaning that the machine is comprised of five identical modules with radial extent $\Delta\varphi = 72^\circ$. In the W7-X naming convention, magnetic modules are assigned a number M from 1 to 5, as demarked with black lines in Fig. 1. Each magnetic module M can be further divided into two stellarator-symmetric half-modules, referred to as $M0$ and $M1$. Here 0(1) identifies the first (second) half of the module when moving anticlockwise in the top-down view of the machine.

Power and particle exhaust within each magnetic module is achieved by employing two stellarator-symmetric divertor units:² one upper divertor and one lower divertor [see Fig. 2(a)]. This gives a total of ten discontinuous divertor units, as visible in Fig. 1. Since the target structures do not extend over the entirety of the magnetic module, two toroidally separated zones can be distinguished: a *divertor region* where most of the plasma-wall interaction takes place, and a *core region* in between the divertor targets (left-hand side and right-hand side of Fig. 3, respectively). The former extends over the bean-shaped symmetry plane at $\varphi = 0^\circ$, which separates the two half-modules, while the latter is centered on the triangular symmetry plane at $\varphi = 36^\circ$.

A large power flux density deposited on the target plates—above the material limits of 10 MW m^{-2} —endangers the target integrity.^{3,4} High target temperatures enhance erosion, shortening the target lifetime, diluting the plasma, and cooling the plasma core. Establishing a detached and highly radiative regime can provide

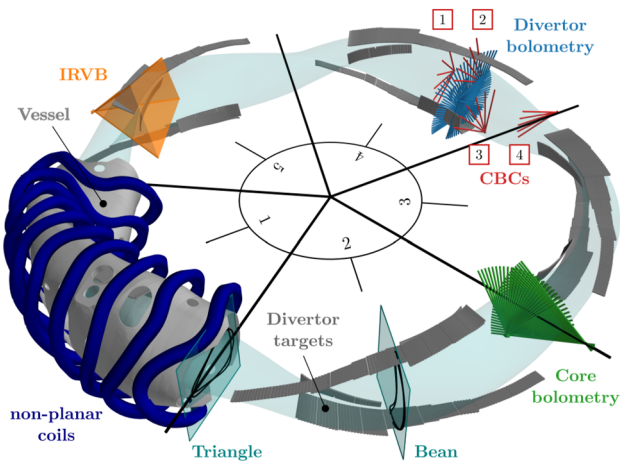


FIG. 1. Current and envisaged bolometer cameras in Wendelstein 7-X: core bolometry (green), divertor bolometry (blue), infrared imaging video bolometry (orange), and CBCs (red, numbered Nos. 1–4). Modules one to five are separated with black solid lines. The divertor targets are included, as are the non-planar coils and vessel structure of module one. One triangular and one bean-shaped symmetry plane are highlighted in teal color.

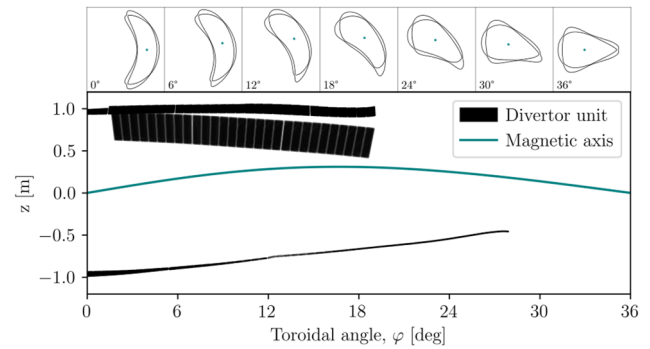


FIG. 3. Coordinates of a divertor unit as a function of toroidal angle φ and vertical coordinate z (derived from Ref. 16). An outline of the island geometry in the standard magnetic field configuration for various toroidal angles is included at the top: 0° corresponds to the bean-shaped cross-section, while 36° corresponds to the triangular plane. The magnetic axis is overlaid in teal color.

a power exhaust solution since the radiation emission is an efficient power dissipation mechanism.^{5,6} The radiated power fraction $f_{rad} = \frac{P_{rad}}{P_{heat}}$ is defined as the ratio of the total plasma radiated power P_{rad} over the total heating power absorbed by the plasma P_{heat} . In a fusion reactor, accurate control of f_{rad} will be required to ensure compatibility of the power exhaust with target material limits. For instance, safe operation of the high fusion gain scenario at ITER will demand a radiated power fraction of at least $f_{rad} = 0.8$.⁷ In this case, P_{heat} is the sum of alpha heating and additional external heating applied to the plasma. At the Demonstration Power Plant (DEMO), an even greater $f_{rad} = 0.95$ will be necessary to optimize the lifetime of the plasma-facing components (65% radiatively dissipated

within the confined volume and an additional 30% in the plasma boundary).^{8,9} To achieve this level of performance, reliably measuring the emissivity profile and the total radiated power, as well as accurate (<5%) control of the plasma radiated power fraction, are of paramount importance.

In the field of high-temperature plasmas, metal foil bolometers are a consolidated diagnostic device for radiated power measurements. More precisely, bolometer detectors measure the absolutely calibrated plasma radiated power, integrated along the detector line-of-sight (LoS).^{10,11} Radiated power measurements at W7-X are currently performed by a combination of resistive and imaging bolometer diagnostics. Figure 2 reports the LoS geometry of all the resistive bolometer cameras, using the same color-coding introduced in Fig. 1. The more consolidated bolometer diagnostic at W7-X consists of a pair of resistive bolometer cameras viewing the triangular symmetry plane between half-modules 21 and 30 (second half of module two and first half of module three).

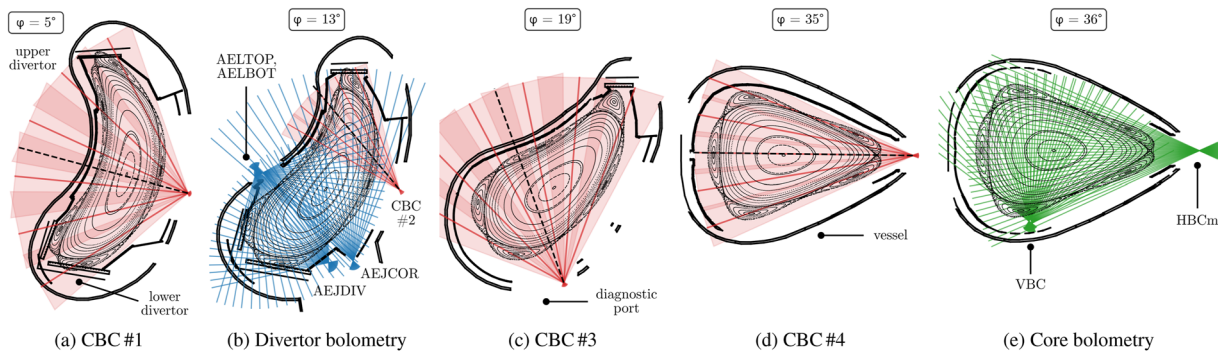


FIG. 2. LoS geometry of the current W7-X resistive bolometer cameras and of the finalized CBC designs. Red cameras are of the CBC type, following the same numbering and color coding as Figs. 1 and 9. (a) CBC No. 1, (c) CBC No. 3, and (d) CBC No. 4 fully cover the plasma poloidal cross-section, while CBC No. 2 complements the (b) divertor bolometry system. The LoS geometry of CBC No. 4 is almost equivalent to HBCm in the (e) core bolometry system. A poloidal cut of the W7-X vessel wall is schematized with black lines, with the half-module-equivalent toroidal angle noted on top. Solid lines identify the central LoS of each channel. For each CBC, the pinhole axis is plotted as a black dashed line, and the 2D projection of the extent of each LoS cone is represented with a colored fan. Areas of darker color indicate regions of overlap between neighboring channels.

This is located in the core region of the plasma, hence the name *core bolometry* system¹² [green, Fig. 2(e)]. The core bolometry system is designed to perform radiation tomography in an up-down symmetric configuration.^{13,14}

More recently, the setup has been upgraded by installing two additional bolometer diagnostics: a *divertor bolometry* system [blue, Fig. 2(b)] and an infrared imaging video bolometer camera, or IRVB (orange). These two are set in the divertor region at the quasi-bean-shaped cross-section in half-modules 40 and 51, respectively (at $\varphi = 13^\circ$ in Fig. 3). Due to the stellarator geometry, the latter two locations are equivalent, but they are flipped upside down with respect to each other in real space. The divertor bolometry system is a set of four resistive cameras offering a higher LoS density on the lower divertor for a more highly resolved radiation front localization in the target interaction region. In addition, the LoS coverage should be sufficient to perform tomographic inversions of the divertor radiation. The IRVB is instead a bolometer of the imaging type.¹⁵ This diagnostic provides a 2D view of the plasma, allowing it to discriminate the emissivity in the toroidal direction.

In a toroidally symmetric machine, a correct estimation of P_{rad} requires a measurement of the average poloidal emissivity. This can be performed without the need to perform tomographic inversions of the radiation distribution. Instead, a proxy for the average emissivity within a bolometer camera field-of-view (FoV) can be obtained by averaging the line-integrated signals with proper geometrical weighting factors [see Eq. (B6)].¹⁴ Still, for this measurement to be possible, the full plasma cross-section in the poloidal plane must be covered by the detection volume of one or more bolometer detectors. This can be achieved with a single fan-shaped array of resistive bolometer foils, such as the horizontal bolometer camera (HBCm)¹⁴ indicated on the right-hand side of Fig. 2(e). However, one implication of the stellarator geometry is the asymmetric distribution of plasma parameters (most notably electron density n_e , electron temperature T_e , and impurity density n_{imp}). As a consequence, radiation emission in a stellarator is expected to follow a 3D pattern.¹⁷ This assumption is supported by experimental and modeling results in W7-X, suggesting the presence of toroidal and up-down poloidal radiation asymmetries, especially in the plasma edge.^{14,18,19} These can be due to volumetric effects, edge asymmetries, and recycling in the target interaction region.^{5,18,20}

In stellarators like W7-X, two main forms of toroidal asymmetries can complicate the task of estimating the total radiated power from a bolometer measurement localized in one poloidal plane. The first kind is an asymmetry within the same half-module, causing a toroidal gradient of the radiated power density along a flux tube. Assuming that stellarator symmetry between different half-modules still holds, this effect can be taken into account by measuring the plasma emissivity at several poloidal cross-sections.²¹ Hence, good LoS coverage of at least one half-module is required to obtain a complete assessment of the 3D structures of the radiative losses. The second kind is an asymmetry between different half-modules or a violation of the stellarator symmetry principle. This symmetry can be broken, for example, by drift effects,¹⁴ error fields,²² or localized seeding of impurities.²³ Experimentally, multiple observations from equivalent diagnostic ports situated in different half-modules can provide validation of the stellarator symmetry principle.

This work introduces a new Compact Bolometer Camera (CBC) concept as a cost-effective solution to assess both the afore-

mentioned kinds of radiated power asymmetries. A CBC is a small-size resistive bolometer diagnostic whose aim is to complement the existing W7-X bolometry setup, which is optimized to provide tomographic capabilities in one specific poloidal cross-section. The CBCs will allow to investigate asymmetries on a large scale, at the expense of spatial resolution. Multiple CBCs can be installed in various toroidal locations to test the assumption of stellarator symmetry and check for the toroidal distribution of radiated power. At the same time, CBCs that are set in a symmetry plane can identify poloidal up-down or in-out asymmetries, depending on their vantage point.

The paper opens with an introduction to the CBC design in Sec. II. An analysis of a set of EMC3-EIRENE²⁴ computed radiation data follows in Sec. III. The simulated data are used to assess the 3D aspects of the plasma radiation distribution. Based on these expected features, the CBC sightline geometry is optimized in Sec. IV. Here, the camera performance results and the improvements in the total radiated power estimate are summarized.

II. THE COMPACT BOLOMETER CAMERA (CBC)

The CBC is a concept for small-size pinhole bolometer cameras with resistive metal foil detectors. A CBC measures the local average poloidal emissivity with just five or six broad LoS while taking advantage of as many diagnostic ports as possible, distributed toroidally throughout the W7-X machine. Furthermore, a CBC can be used to complement an already existing bolometer system by introducing more bolometer sightlines in plasma regions lacking sufficient coverage. For this purpose, the camera design has to be inexpensive, easily applicable to many of the port viewing geometries, and compact to require minimal port space. This is achieved by reducing the camera concept to its essential components, highlighted in Fig. 4: detectors, protective housing, and electrical connection to deliver the acquired signal to the measurement units. More details regarding the engineering of the CBC design can be found in Appendix A.

We propose four new CBCs for four different diagnostic ports in half-module 40, whose locations are numbered 1 to 4 in Fig. 1. Their respective sightline geometries are visualized in red color in Fig. 2. CBCs Nos. 1, 3, and 4 will be used to estimate the local average poloidal plasma emissivity. All these CBCs will cover the full plasma poloidal cross-section, each at their respective toroidal location. CBC No. 1 [Fig. 2(a)] and CBC No. 3 [Fig. 2(c)] measure near the bean-shaped symmetry plane and the tear-shaped cross-section, respectively. CBC No. 4 [Fig. 2(d)] provides a LoS coverage of the triangular symmetry plane that is almost equivalent to HBCm [Fig. 2(e)]. These three cameras together will yield toroidally resolved measurements of the average poloidal plasma emissivity over the larger portion of a half-module. On the other hand, CBC No. 2 [Fig. 2(b)] will complement the divertor bolometry system. The five new sightlines will provide additional coverage in the upper divertor area where the LoS density is the lowest and a secondary vantage point to better separate the local emissivities. This translates to lower inversion errors and improved tomographic capabilities (quantifying this improvement will be the scope of future work and is not discussed here).

Each CBC consists of a protective box, housing five or six resistive bolometer foils, temperature sensors, and the necessary

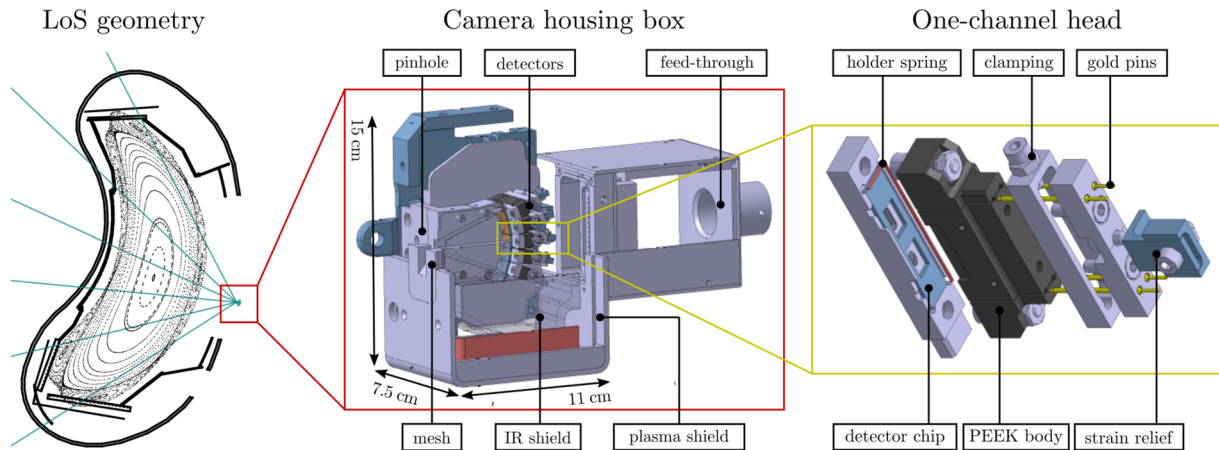


FIG. 4. (Left) Central lines-of-sight of CBC No. 1 superimposed to a Poincaré plot of the W7-X standard magnetic configuration and a cut of the vessel walls ($\varphi = 5^\circ$). (Center) Main components of the CBC housing and (right) exploded view of the one-channel bolometer head. The inexpensive and flexible design facilitates installation in multiple diagnostic ports.

cabling. In the CBC design, each bolometer LoS is implemented as a newly designed one-channel head, improving the flexibility of the LoS geometry. A rendered image of the one-channel head design is reported in Fig. 4 right-hand side and Fig. 15. The detector elements themselves are identical and directly comparable to the already established resistive bolometer chips.^{10,14} However, the detection solid angle as well as the signal-to-noise ratio are increased by widening the pinhole and reducing its distance to the detectors. This way, a very large FoV angle can be achieved to provide full coverage of the plasma poloidal cross-section with just a few channels (see Fig. 2 and the left-hand side of Fig. 4). For example, in the core bolometry system [see Fig. 2(e)], the triangular cross-section is fully covered by HBCm with a total of 32 sightlines. An equivalent full coverage can be obtained by a single compact camera—CBC No. 4 [see Fig. 2(d)]—mounting only five channels. At the same time, the lower LoS collimation causes poorer spatial resolution.

The housing box containing the CBC detectors is installed in the W7-X cryostat through one of the available diagnostic ports.²⁵ In the core and divertor bolometry systems, this is performed by mounting the detector heads on the far end of a ~2 m long immersion tube, which provides shielding and support. The immersion tube also carries all the necessary cabling for signal acquisition, as well as the pipes for the pneumatic shutter actuation and the water cooling. Once assembled, it is slid into the cryostat from the outside, plugging the port.¹² For example, the set of four cameras composing the divertor bolometry system [blue lines in Fig. 2(b)] are mounted on two separate immersion tubes. Using the W7X port names, every port is identified by a specific three-letter acronym followed by the half-module number. One of the two immersion tubes plugs the AEJ40 port (AEJ port of half-module 40) and mounts the two out-board cameras AEJCOR and AEJDIV. The second one plugs into the inboard port AEL40, hence the names of the two cameras, AELBOT and AELTOP. A Computer-Assisted Design (CAD) drawing of the latter immersion tube is reported in the lower panel of Fig. 5. The electronic cables (for the temperature sensors and the bolometer detectors) are missing from this picture.

Contrarily to the core and divertor bolometry systems, a CBC includes no pinhole shutter mechanism and no active cooling system, as shown in the upper panel of Fig. 5. This, together with the reduced number of channels, allows for a more simplified and lightweight design of the detector housing box and cable feed-through pipe. By fixing these directly on the water-cooled diagnostic port liner, the necessary mechanical stability and heat sink can be achieved without the need for an immersion tube. Foregoing, the diagnostic immersion tube considerably reduces the needed port space, design cost, and complexity. At the same time, the dimension of the housing box (10–20 cm, as shown in the central panel

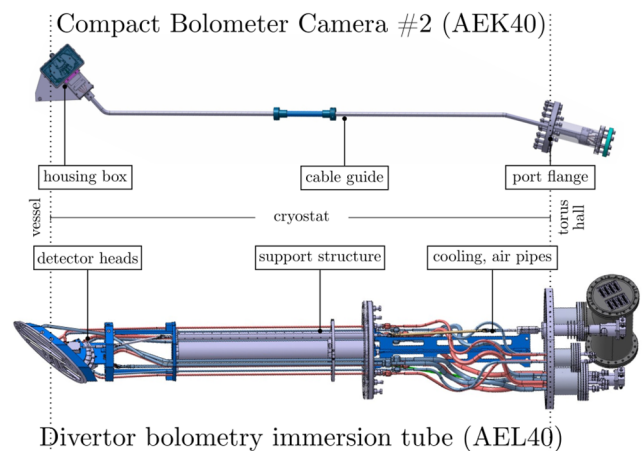


FIG. 5. Comparison between the design of (upper) CBC and (lower) one immersion tube of the divertor bolometry system. Their sightline geometries are reported in Fig. 2(b) as CBC No. 2 and AELBOT/AELTOP, respectively. Dotted lines set the boundaries of the three different zones, from outermost to innermost: torus hall, cryostat, and plasma vessel.

of Fig. 4) is typically considerably larger than the W7-X diagnostic ports—hence the name “compact.” Since the port is not plugged by an immersion tube, and given the contained size of the housing and feed-through components, a CBC can be installed alongside other diagnostics and share the port space.

For reference, CBC Nos. 1–4 are assigned to the four ports AEE40, AEK40, AEM40, and AEU40, respectively. Both the CBC housing and cable feed-through are modular and can, therefore, be manufactured in series and efficiently adapted to any of the W7-X diagnostic ports. For each port geometry, the camera design can be adapted by studying its synthetic response to plasma radiation, which in this study is modeled using a ray tracing routine. This step can be repeated for many different iterations of the CBC design to determine the optimal camera geometry, as will be discussed in Sec. IV A.

III. EMISSIVITY DISTRIBUTION

This section identifies a set of radiation phantoms that we can employ in Sec. IV A to optimize the CBC design based on the synthetic camera response. These have to reflect the most commonly observed radiation features in W7-X. We begin with some simplified mock-ups in Sec. III A, while Sec. III B treats phantoms from simulations. Only the standard magnetic field configuration is discussed here.²⁶

A. Mock-up radiation phantoms

Recent experimental studies on the 2D radiation profile at W7-X have uncovered consistent plasma behavior depending on the electron density n_e and the radiated power fraction f_{rad} .¹⁴ Most notably, at relatively low density and low f_{rad} , the plasma radiation profile tends to be hollow, peaked at the plasma edge, and with an almost uniform poloidal distribution (so-called “ring” pattern).¹⁴ On top of this, a broader and low-intensity cloud of radiation can sometimes be observed in the confined region around the magnetic field axis. This is associated with the penetration of impurities and neutral hydrogen.^{14,27,28} At higher density and f_{rad} , the island structure starts to emerge, with radiation peaking close to the X-point locations.¹⁴ An overall up–down asymmetry in the radiation intensity appears as well, with the lower X-points radiating more (less) than the upper ones in forward (reversed) field polarity.¹⁴ Furthermore, during radiation collapse events, the plasma can shrink to approximately half of its original volume. This phenomenon—often referred to as “small plasma”—is accompanied by a significant amount of core emission and the movement of the radiation front radially inside the Last Closed Flux Surface (LCFS).^{27,29}

Based on these findings, a set of six representative mock-up phantoms is defined. As reported in Fig. 6, these represent, respectively,

- constant emissivity ring,
- up–down asymmetric ring,
- up–down asymmetric ring,
- core emission,
- small plasma and,
- up–down asymmetric ring with core emission.

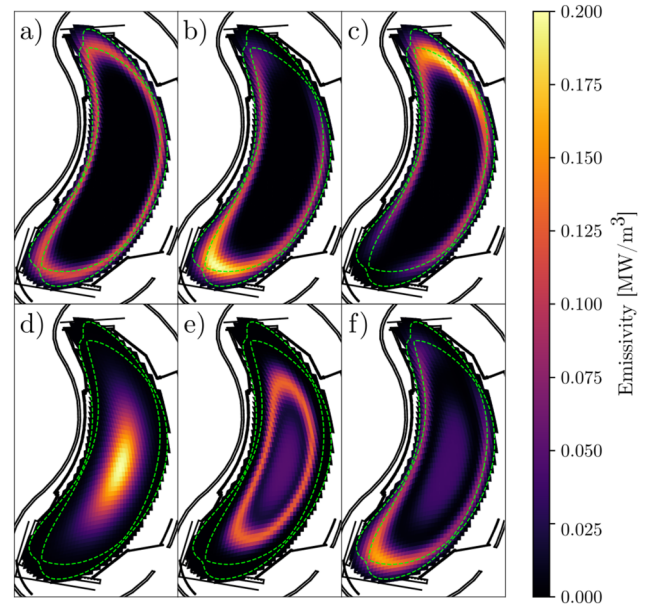


FIG. 6. Mock-up phantoms of the plasma emissivity employed in the optimization process. The magnetic island structure is indicated with a dashed green line. These phantoms represent the most common broad features observed experimentally: poloidally (a) symmetric and [(b), (c), and (f)] asymmetric rings, (d) core emission, and (e) small plasmas. Each phantom is given the same weight in the procedure.

The mock-up radiation distributions in the poloidal plane are generated using functions of the radial and poloidal coordinates of the magnetic equilibrium obtained from the Variational Moments Equilibrium Code (VMEC).³⁰ The functions used are Gaussian functions with different characteristic radial/poloidal lengths to control the smoothness and symmetry of the radiation rings. The associated total P_{rad} of each mock-up phantom is ~ 1 MW.

B. EMC3-EIRENE radiation phantoms

Carbon radiation is the main contributor to radiative power losses in W7-X.²⁸ This is especially true after wall boronization, which suppresses oxygen and other impurities.²⁸ In order to apply radiation phantoms that are as realistic as possible, we employ EMC3-EIRENE²⁴ simulations of the plasma radiation from the dominant low-Z carbon impurity.^{24,27,31} Each simulation is set in standard magnetic field configuration, with varying set values for the particle diffusion coefficient D ($\text{m}^2 \text{s}^{-1}$), heat diffusion coefficient χ ($\text{m}^2 \text{s}^{-1}$), radiated power P_{rad} , applied heating power P_{heat} , and separatrix electron density n_{sep} (m^{-3}). For all the following cases, the latter two are set to $P_{heat} = 5$ MW and $n_{sep} = 3 \times 10^{19} \text{ m}^{-3}$. The heat diffusion coefficient is scaled with the particle diffusion coefficient so that $\chi = 3D$.^{32,33}

The emissivity per voxel due to each impurity species Z_{imp} is calculated from the computed impurity ion density n_{imp} , electron density n_e , and temperature T_e local information using

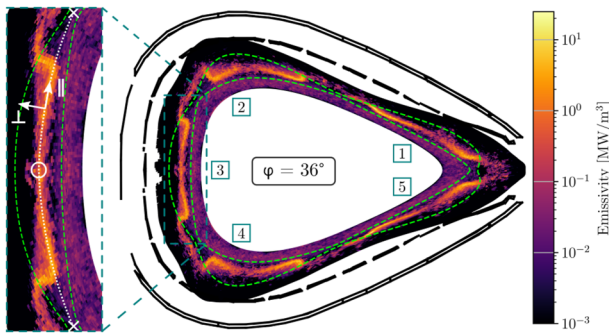


FIG. 7. Poloidal distribution of the radiated power density from carbon impurities in the symmetrical triangular plane, simulated by the EMC3-EIRENE code. The core bolometry system is located at this toroidal angle [see Fig. 2(e)]. Each island is numbered one to five following the VMEC poloidal coordinate. Emission from the inboard island is enlarged on the left-hand side with the island O-point and X-points highlighted.

$$\epsilon(n_e, T_e) = n_e \sum_{z=0}^{z_{imp}-1} n_{imp, z} L_z(n_e, T_e). \quad (1)$$

Impurity atomic data are also required in the form of a radiation loss function L_z , taken from the Atomic Data and Analysis Structure (ADAS) system.^{34,35}

Across all the studied simulations, some consistent features are identified: the overall distribution of the plasma emissivity near the separatrix is flux surface aligned, with stronger gradients in the radial direction compared to the poloidal one. Figure 7 reports a typical EMC3-EIRENE emissivity distribution in the triangular plane (note the logarithmic scale of the color map). Due to the relatively large temperatures inside the confined region, the carbon impurity radiation is predominantly located in the cooler edge and islands. Most of the radial heat flux entering the Scrape-Off Layer (SOL) is diverted by the parallel transport, causing the radiation front in the SOL to follow a radially extended separatrix (white dashed line on the left-hand side of Fig. 7). The intensity of the radiation front peaks in between each island O-point and the two X-points. Approaching the

X-point, the magnetic field pitch angle decreases, and the orientation of the radiation front changes from predominantly parallel to the extended separatrix to predominantly perpendicular to it (pointing radially outward).^{36,37}

In this study, we utilize a regular EMC3-EIRENE that extends over one stellarator half-module ($\Delta\phi = 36^\circ$). The 3D structure of the grid is aligned with the magnetic field direction and with the confined flux surfaces (separatrix), allowing the definition of a radial, poloidal, and toroidal index for each voxel based on the magnetic coordinates. The grid radial and poloidal direction is aligned with the “unperturbed” flux surfaces; hence, the magnetic island flux surfaces are missing. However, the parallel structure is respected by the alignment with the magnetic field. In this case, the grid presents 139 sections in the radial direction, 512 sections in the poloidal direction, and 36 sections in the toroidal direction. By taking advantage of this indexing, we can average the emissivity in different directions, generating profiles of the radiation distribution. Since the radiated power contribution of each voxel is given by the product of its radiated power density and associated volume, this average is weighted using the individual voxel volumes as weights.

We begin by averaging together all the voxels in the poloidal and toroidal directions, collapsing the distribution on the effective minor radius coordinate. The obtained 139 points that define our average radial profile of the carbon radiation are plotted in Fig. 8(a). As D and χ increase in the simulations (dashed lines), the radial and poloidal gradients of the emissivity spatial distribution tend to be smaller. At the same time as the emissivity profiles are smoothed out, the radiation front peaking location is shifted inwards toward the separatrix. A similar smoothing applies to the poloidal and toroidal profiles, which are discussed later [Figs. 8(b) and 9]. However, for $D = 0.2\text{--}0.5 \text{ m}^2 \text{ s}^{-1}$, the finest peak structures are still below the average spatial resolution of bolometer LoS of $\sim 3 \text{ cm}$. Focusing on the radiated power fraction dependence, at lower (higher) D , the radial width of the averaged radiation peak is reduced (increased) at larger f_{rad} . As f_{rad} approaches unity, the low-temperature region with conditions for efficient low-Z radiation moves toward the separatrix. These effects are consistent with detachment physics and simulations from previous publications.^{36,37}

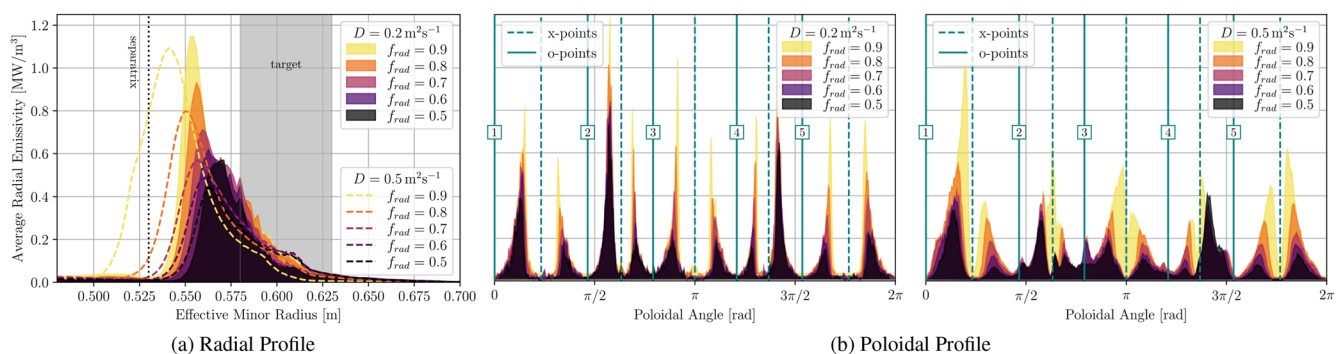


FIG. 8. (a) Radial profile of the EMC3-EIRENE emissivity distribution of carbon radiation. The radial position of the plasma separatrix is indicated with a dotted vertical line, and the divertor target intersection area (at $\varphi = 0^\circ$) is grayed out. (b) Poloidal profiles of the EMC3-EIRENE emissivity distribution of carbon radiation at (left) lower and (right) higher diffusivity. The location of the five island X- and O-points in the poloidal direction is represented with teal dashed and solid lines, respectively. The island numbering is consistent with Fig. 7. The radiation front movement with increasing f_{rad} toward the separatrix and toward the X-points is accentuated at higher diffusivity.

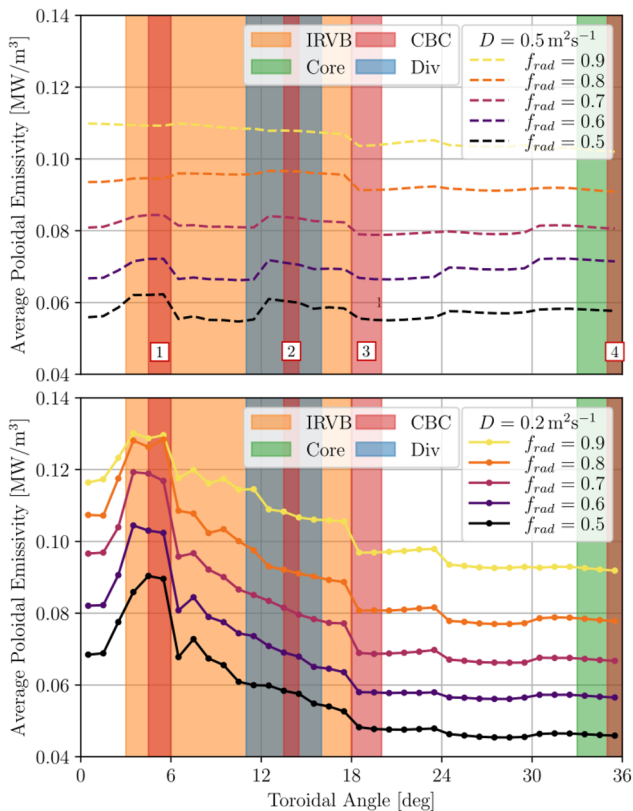


FIG. 9. Toroidal profiles of the EMC3-EIRENE emissivity distribution of carbon radiation at (upper panel) high and (lower panel) low diffusivity. The coverage provided by each bolometer camera is indicated by color bands, using the same color-coding as in Fig. 1: green for core bolometry (Core), blue for divertor bolometry (Div), red for the CBCs (numbered 1–4 in the upper panel), and orange for the IRVB. The degree of toroidal asymmetry over a half-module is enhanced in the lower diffusivity cases.

A similar behavior is observed in the poloidal profile of the carbon radiation, shown in Fig. 8(b). Here it is possible to identify ten local emission maxima, or two per one of the five islands. In this case, the ten emissivity peaks shift away from the island O-points toward the island X-points at higher D or f_{rad} , while their FWHM is reduced. This movement is accentuated at higher diffusivity, to the point where each two neighboring maxima nearly merge at the X-point. Although condensation of the radiation around the X-point at high radiated power fraction has been consistently observed during experiments, its details are still to be understood.^{14,27}

Notably, since drifts are not included in the EMC3-EIRENE code, significant deviations from the experiment are expected. For example, the poloidal profile of the plasma emissivity is exactly up-down symmetric in the two symmetrical cross-sections: the triangular plane and the bean-shaped plane. As the poloidal profile presented in Fig. 8(b) is averaged over a half magnetic period, an apparent asymmetry arises such that plasma radiation from the upper—1, 2—and lower—4, 5—islands is not identical. This

is purely caused by the asymmetric nature of one individual half-module and is not to be confused with the experimentally observed up-down asymmetry,¹⁴ which is not captured by EMC3-EIRENE.

Finally, we observe a non-uniform toroidal distribution of the SOL carbon radiation inside a 3D flux tube. As reported in Fig. 9, the consequence is a considerable gradient of the average poloidal emissivity in the toroidal direction. The toroidal asymmetry is accentuated for low radiated power fraction (darker colored lines) and low diffusivity (lower panel). In the $D = 0.2 \text{ m}^2 \text{ s}^{-1}$, the value most commonly used at W7-X,³² the variation is up to $\pm 30\%$. The radiated power density is found to be the highest in the divertor region, where the main plasma-wall interaction happens. The poloidal average emissivity peaks within $\varphi = 0^\circ\text{--}18^\circ$, consistent with the location of peak heat deposition on the target.³⁸ In the higher diffusion cases (higher panel), the maximum variation is a much lower $\pm 5\%$. Notably, the plasma volume in each poloidal cross-section, including the magnetic islands, varies by only $\pm 1\%$ as a function of the toroidal angle. This means that the change in radiated power density is not a volumetric effect but is rather driven by a non-uniformity in the plasma parameters such as electron density, temperature, and concentration of a given impurity charge state. All the aforementioned parameters vary along the toroidal direction.

Such a prominent toroidal asymmetry means that the total plasma radiated power can be significantly under or overestimated when it is—toroidally—extrapolated from a local bolometer measurement [see Eq. (B6)]. This extrapolation error would in turn lead to large global power balance errors. Attempts to correct for it have so far been limited to the inclusion of a fixed re-scaling factor assessed through modeling, which depends on magnetic field geometry and plasma conditions.³⁹ Alternatively, a trained weighted average of the individual line-integrated emissivities could be applied.⁴⁰

Based on the EMC3-EIRENE predictions, experimentally we should observe large deviations when comparing the average emissivity measured by several toroidally separated bolometer diagnostics. With the current setup, this variation is expected to be significant across the IRVB view, in the toroidal direction ($\varphi = 5^\circ$ to $\varphi = 18^\circ$ in Fig. 9). Moreover, a comparison between CBC No. 1 ($\varphi = 5^\circ$) and CBC No. 4 ($\varphi = 35^\circ$) measurements should exhibit a large discrepancy in this sense. This information would be crucial not only to understand the behavior of 3D radiation asymmetries as a function of plasma parameters but also to improve our current estimation of the global radiated power. The improved coverage, depicted in Fig. 9, will provide new information on the degree of toroidal variation of the emissivity.

It can be noticed from Fig. 9 right-hand side that the CBC No. 4 sightlines overlap with the core bolometry system, making its measurement of the average plasma emissivity redundant. However, as mentioned at the end of Sec. II, the LoS coverage from CBC No. 4 is almost equivalent to the one of HBCm [compare CBC No. 4 in Fig. 2(d) with HBCm in Fig. 2(e)]. This provides an equivalent measurement from a different magnetic module that can be directly used to validate the stellarator symmetry principle.

In order to include these radiation features predicted by the EMC3-EIRENE code, three simulated radiation phantoms are selected for the geometry optimization procedure described in Sec. IV A. Following the numbering reported in Fig. 10, they correspond to

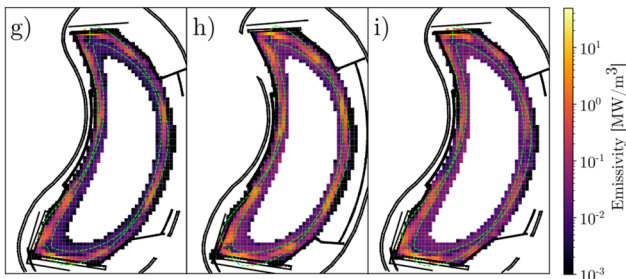


FIG. 10. EMC3-EIRENE phantoms of the plasma emissivity employed in the optimization process, mapped on the regular ray tracing grid. These phantoms complement the set of mock-ups reported in Fig. 6 and represent the three cases: (g) low D and low f_{rad} , (h) low D and high f_{rad} , and (i) high D and low f_{rad} . Notice the logarithmic color bar scale.

- (g) $D = 0.2 \text{ m}^2 \text{ s}^{-1}$, $f_{rad} = 0.5$,
 (h) $D = 0.2 \text{ m}^2 \text{ s}^{-1}$, $f_{rad} = 0.9$ and,
 (i) $D = 1.0 \text{ m}^2 \text{ s}^{-1}$, $f_{rad} = 0.5$.

A value of $D = 0.2 \text{ m}^2 \text{ s}^{-1}$ is chosen for the diffusion coefficient, with an intermediate and a high radiated power fraction case. The choice of D is based on previous studies and comparisons between experiments and modeling.³² A third $D = 1.0 \text{ m}^2 \text{ s}^{-1}$ simulation is used as a comparison at high diffusivity. The calculated emissivity values are interpolated from the EMC3-EIRENE simulation grid to the same 3D mesh used for the mock-up radiation phantoms shown in Fig. 6, the latter presenting a much coarser voxel size. This difference in spatial resolution is evident when comparing the emissivity distributions reported in Figs. 7 and 10.

IV. RESULTS AND DISCUSSION

This section details the modeling of the CBC response and the expected performance of each camera. Section IV A describes the main parameters determining the LoS geometry and how they are optimized. In Sec. IV B, the final CBC designs are tested in terms of their capability to identify poloidal and toroidal asymmetries.

A. CBC geometry optimization

By taking advantage of a fast ray tracing routine, we can scan over many LoS geometries and assess the camera response. To simplify camera design and construction, we set a constant focal length for all detectors and a symmetric placement of the detector fan relative to the pinhole axis, or the vector normal to the slit surface and centered on its centroid (black dashed lines in Fig. 2). We optimize the four CBC designs in terms of their location, pinhole size, focal length d , and aperture angle of the camera FoV θ . The latter two quantities, respectively, correspond to the distance between detectors and pinholes and the angle between the two outermost LoS. These variables are schematized in Fig. 11 for a detector fan and in Fig. 15 for a single detector. See Appendix B for more details on the detector-to-pinhole geometry.

First, the camera location and orientation are set so as to center the view on the magnetic axis, as much as allowed by the port geometry. Second, the toroidal and poloidal extent of the viewing

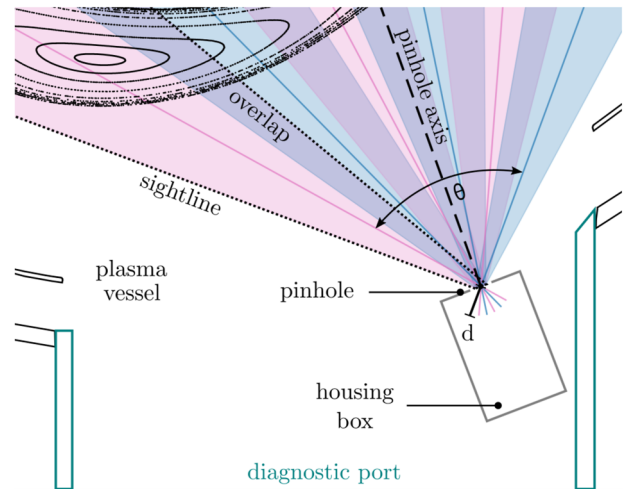


FIG. 11. Schematic representation of the variables taken into account during the CBC geometry optimization: housing box location in the diagnostic port, pinhole size, orientation of the pinhole axis, focal length d , aperture angle of the detector fan θ , overlap of sightlines. This is a closeup on CBC No. 3, whose full cross-sectional view can be seen in Fig. 2(c). Different LoS are represented with alternating pink and blue colors.

cone is regulated by acting on the slit width and height (see Fig. 15), while the orientation of the LoS fan is dictated by the port axis (the CBC is fixed on the port liner wall and, therefore, aligned with the port direction). Then, an upper limit θ_{max} and a lower limit θ_{min} are manually determined to avoid either cropping of the LoS from the machine walls ($\theta > \theta_{max}$) or partial coverage of the poloidal cross-section ($\theta < \theta_{min}$). Once the range of accepted θ values is fixed, a maximum allowable distance d_{max} is singled out such that for $d < d_{max}$, each configuration in the chosen θ range has non-zero overlaps of the LoS cones (see sightline highlighted in Fig. 11). Because of the finite physical size of each detector head, a minimum achievable distance d_{min} is also defined based on engineering constraints. Finally, an automatic configuration scan is performed over every combination between the two ranges $[\theta_{min}, \theta_{max}]$ and $[d_{min}, d_{max}]$.

For a specific CBC configuration (i.e., detector and pinhole coordinates), the geometry matrix G is traced using Cherab,⁴¹ and the length d_{LoS} and volume V_{LoS} of the LoS intersection with the plasma is computed. In this case, a lower number of 10^4 random rays is used for the tracing to improve speed (order of 1 s of runtime per detector on a local machine) at the cost of geometry matrix accuracy.

To further speed up the optimization process, the plasma emissivity is assumed to be constant along the magnetic field lines, which reduces the forward model from a 3D problem to 2D. In practice, this requires interpolating the 3D geometry matrix on a field-aligned three-dimensional grid. By summing up all the values along the toroidal direction, the geometry matrix is collapsed to a 2D grid in the poloidal plane. This is the grid on which phantoms and geometric factors are displayed in Figs. 1, 6, and 16(b). Ignoring toroidal variations is justified since each CBC considered in this study presents a FoV that is mostly aligned with the poloidal

plane and, therefore, provides no toroidal resolution in the individual CBC measurement. The reader can find more information on the geometry matrix and the ray tracing routine in [Appendix C](#).

For each of the nine phantoms—letters (a)–(i)—selected in Sec. III, we use Eq. (B8) to forward calculate the synthetic measurements p of the radiated power line-integrated on the CBC channels. The absorbed power p on a given channel can be normalized to the LoS geometry with B4, obtaining the chord brightness measurement ϵ_{chord} (W m^{-3}).¹⁴ The chord brightness is essentially a measure of the plasma emissivity, averaged within the FoV of a detector. When multiple LoSs are employed to estimate the average plasma emissivity in the FoV, all the chord brightness values are averaged together with their respective LoS volumes V_{LoS} as weights [Eq. (B5)]. When this procedure is applied to a detector fan aligned with the poloidal plane such as CBC Nos. 1, 3, or 4 (shown in [Fig. 2](#)), it yields an estimate for the local average poloidal emissivity $\langle \epsilon \rangle$ of each phantom. These can be extrapolated to the whole plasma volume with Eq. (B6) to obtain the total radiated power P_{rad} .¹⁴ As mentioned in Sec. I, this method for estimating a P_{rad} proxy solely relies on averaging the line-integrated data with adequate weighting factors.

A reference forward measurement is then performed for a larger 32-channel bolometer camera that resembles the LoS setup of HBCm from the core bolometry system [depicted in [Fig. 2\(e\)](#)]. We choose HBCm as a reference since it is currently the source of the P_{rad} proxy signal in W7-X.²⁷ The reference (HBCm-like) camera has the same LoS etendue and geometry as HBCm, but the camera axis is translated and rotated to have the same pinhole axis and location and camera orientation as the CBC (indicated in [Figs. 2](#) and [11](#)). This reference represents the most favorable coverage of the diagnostic port under consideration. An example of the two modeled responses for CBC No. 1 and its reference is shown in [Fig. 13](#).

It is found that both the CBC and the reference camera P_{rad} proxy misrepresent the real radiated power by a significant amount. The discrepancy depends on the camera and on the phantom under investigation, but it is usually in the order of 10% for the phantoms introduced in Sec. III. Symmetric mock-up phantoms are often assessed with higher accuracy. Conversely, asymmetric mock-up phantoms and EMC3-EIRENE phantoms yield the largest errors, which can be as high as 20%–25% in the worst cases. Since the toroidal variations of the plasma emissivity are not included, the discrepancy is caused by imprecisions in the estimation of the average poloidal emissivity $\langle \epsilon \rangle$. Including the toroidal variation reported in [Fig. 9](#) would introduce an additional source of error with respect to the true P_{rad} value due to the localized nature of the camera measurement.

The relevant information here is how far the lower spatial resolution of the CBC leads to a degeneration of the P_{rad} proxy compared to a high-resolution reference system. Therefore, a comparison is made with the full 32-channel reference camera and not with the true total radiated power value. We express the overall discrepancy between a CBC and its reference as a percentage error averaged over all nine radiation phantom cases with equal weights. This case-averaged error is the quantity to be minimized to achieve geometry optimization, as shown in the geometry scan in [Fig. 12](#).

While the case-averaged error between the camera proxy and the exact total P_{rad} value can be of the order of 10%–20%, we find that the CBC estimate and the reference estimate can be in much better agreement. The average mismatch between the two is, in

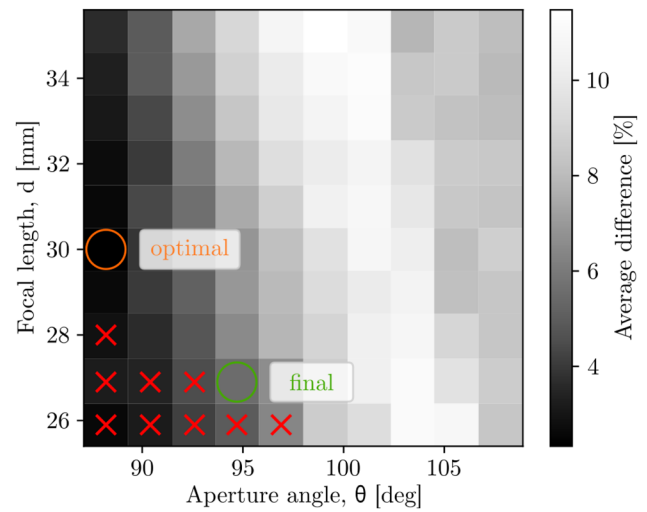


FIG. 12. Geometry scan for CBC No. 1 over different camera aperture angles θ and focal lengths d . The color map represents the P_{rad} proxy discrepancy compared to an equivalent 32-ch. camera reference, averaged over all nine phantom cases. Red crosses indicate the configurations that are impossible to build. With the right configuration, a difference $< 5\%$ can be achieved. The optimal configuration is circled in orange, and the final one in green.

some instances, smaller than 5%. This means that with the right LoS geometry, a CBC can provide a relatively reliable proxy for the total radiated power measurement.

The case-averaged percentage error as a function of camera aperture angle and focal length is often distributed in regions of maxima and minima. As shown by [Fig. 12](#), the optimal configuration of LoS geometries sometimes falls in the bottom-left corner at very low d and θ . Depending on the engineering constraints on the minimum head-to-head distance, some designs with these characteristics cannot be realized (red crosses in [Fig. 12](#)). This requirement is somewhat relaxed at larger θ values because a wider opening of the detector fan makes more space for placing the one-channel heads side by side.

Moving to geometries with large d and θ , corresponding to the top-right end in [Fig. 12](#), the overlap between the LoS cones tends to reduce. This deteriorates the proxy P_{rad} calculation, giving rise to the high error band crossing [Fig. 12](#) diagonally from the bottom right to the upper left. In some cases, at even larger θ angles, the inner lines of sight might compensate for the edge channels moving out of the plasma volume. The compensation creates then a second band of configurations with a slightly better match, visible on the right-hand side of [Fig. 12](#). These geometries are however prone to blind spots due to the very localized and spaced-out LoSs, offering a less robust performance. For this reason, after the optimal CBC design is identified by picking a LoS geometry within the optimal and buildable region, it must be manually checked for good LoS overlap. For the case of CBC No. 1, the optimal configuration (orange circle) leads to some blind spots with no overlap between the edge channels. A finite overlap is ensured by reducing the focal length d , which at the same time requires increasing the aperture angle θ to relax the manufacturing constraints. This places the final configuration in the region encircled in green in [Fig. 12](#).

TABLE I. Geometrical parameters of the compact bolometer cameras and their reference (HBCm). These parameters are visualized in Fig. 11. The LoS spatial resolution in the poloidal plane varies depending on the distance to the pinhole.

Camera	Pinhole (mm)	Focal length d (mm)	Aperture angle θ (deg)	Etendue ($\text{m}^2 \text{sr}$)	Spatial resolution (cm)
CBC no. 1	12×5	27	95	8.6×10^{-8}	10–40
CBC no. 2	8×5	48	40	2.0×10^{-8}	5–12
CBC no. 3	12×5	32	80	6.3×10^{-8}	10–35
CBC no. 4	8×5	48	40	2.0×10^{-8}	5–30
HBCm	5×10	176	52	1.9×10^{-9}	1–5

The final CBC LoS geometries resulting from the optimization are displayed in Fig. 2, next to the pre-existing cameras from the divertor and core bolometer systems. CBCs Nos. 1, 3, and 4 were optimized through geometry scans such as the one reported in Fig. 12. CBC No. 2 is not meant to provide a P_{rad} proxy but is instead complementary to the divertor system. Its housing is a clone from CBC No. 4, adapted to the different port geometry and rotated to cover the region with the lowest LoS density. We find that, for the chosen camera locations of CBCs Nos. 1 and 3, coverage of the whole plasma cross-section requires a wide aperture angle and LoS width. The resulting LoS overlaps (darker shaded regions in Fig. 2) are significant, especially for channels close to the camera axis. This could be solved by increasing the focal length of the middle channels, which would make their sightlines more collimated (but complicate construction).

Table I lists the final geometrical parameters of the four CBCs and HBCm. The pinhole size (first column) of the CBC cameras is generally larger, and the focal length d (second column) is shorter compared to the HBCm reference. This amounts to approximately a 10- to 20-fold increase in the detector etendue [see Eq. (B3)] and, therefore, a much larger signal-to-noise ratio on the CBC channels. For a 1 MW radiation phantom, the incident line-integrated power on an HBCm detector is of the order of $p = 0.02$ mW, while it is $p = 0.2$ mW for the equivalent CBC No. 4. CBCs Nos. 2 and 3 have the largest etendue, and their measured incident power is, respectively, of the order of 0.3–0.4 mW per MW of total plasma radiated power.

Table I also reports the spatial resolution of the CBCs in the poloidal plane (fifth column), which here is taken as the distance between the central sightline of adjacent bolometer channels at a given point in space. The first listed number is the spatial resolution at the crossing point to the plasma volume close to the pinhole [e.g., right-hand side of Fig. 2(a)]. The second listed number corresponds to the second crossing point, further away from the pinhole [e.g., left-hand side of Fig. 2(a)].

B. CBC performance

Once the optimal geometry of each CBC is established, its design can be finalized and its performance can be predicted in more detail. We start with the capability of the CBC concept to sort out poloidally symmetric patterns from asymmetric ones.

In the case of a symmetric bolometer camera setup like HBCm [see Fig. 2(e)], the profile of the camera measurement is expected

to be precisely symmetrical when viewing a uniform radiation ring—e.g., Phantom (a) in Fig. 6. Depending on the camera vantage point, the profile can become asymmetric when the radiation distribution is either up–down or in–out (inboard–outboard) asymmetric.¹⁴ Despite CBC No. 1 not being exactly oriented with the midplane in the bean-shaped cross-section [see Fig. 2(a)], its LoS geometry is sufficiently symmetrical to provide a good example for this principle. The asymmetry of LoS volume and geometry of a CBC can be partly addressed with correction factors, which are not applied here.

Figure 13 upper panel shows the forward calculated response of CBC No. 1 to Phantom (a), expressed as chord brightness ϵ_{chord} . The ratio of upper to lower channels gets skewed when moving to a top-down asymmetrical ring like Phantom (b), as shown in Fig. 13 lower panel. The conclusion is that CBC is able to identify poloidal asymmetries. Due to its particular vantage point from the outboard side, CBC No. 1 is only capable of discerning an up–down asymmetry of the radiation pattern. To identify in–out poloidal asymmetries, a CBC measuring from an upper port or a lower port [e.g., Vertical Bolometer Camera (VBC) in Fig. 2(e)] would be necessary.

The second criterion that is relevant for evaluating the CBC performance is its ability to reliably estimate the poloidally averaged local emissivity. This can be assessed by comparing the radiated power proxy based on the camera measurement [Eq. (B6)] to the voxel sum of the plasma emissivities. The scope of this test is to evaluate to what extent multiple CBCs in several toroidal locations can trace the toroidal emissivity profile and how this information can be used to improve the P_{rad} proxy. We consider CBCs Nos. 1, 3, and 4 for this test.

The synthetic response to three of the EMC3-EIRENE radiated power phantoms introduced in Sec. III is analyzed. We choose the three cases at $f_{rad} = [0.5, 0.7, 0.9]$ and $D = 0.2$ ($\text{m}^2 \text{s}^{-1}$) shown in the lower panel of Fig. 9. The synthetic line-integrated measurement is forward calculated based on the three-dimensional EMC3-EIRENE radiation distribution, so that each camera response derives from the toroidally resolved plasma radiated power. Again, we use the camera measurements to estimate the local average poloidal emissivity, which is calculated as the V_{LoS} -weighted average of the chord brightness [Eq. (B5)]. Figure 14 compares the toroidal distribution of the average poloidal emissivity (dashed lines) with the CBC estimate (solid lines) for the three cases. The toroidal profiles of the phantoms are calculated following the same method as in Fig. 9.

The results show significant differences between the three CBC responses, with a trend that roughly resembles the toroidal profiles

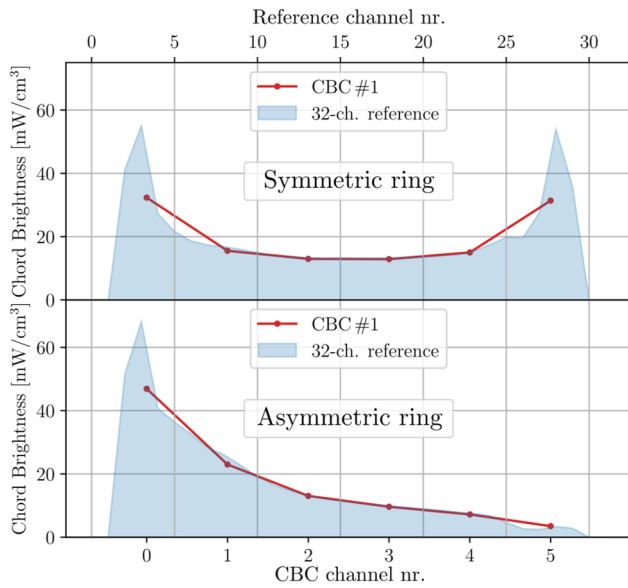


FIG. 13. Synthetic chord brightness measurement calculated for optimal CBC No. 1 geometry and the associated 32-ch. reference, corresponding to two different mock-up phantoms: (upper) a symmetric ring and (lower) an up-down asymmetric ring. The two phantoms are labeled (a) and (b), respectively, in Fig. 6. Lower channel numbers cover the lower part of the plasma.

introduced in Fig. 9. The CBC-estimated average poloidal emissivity presents a lower asymmetry degree for the highest f_{rad} case, which is in agreement with the behavior described in Sec. III. For these three phantoms, CBC No. 1 appears to consistently

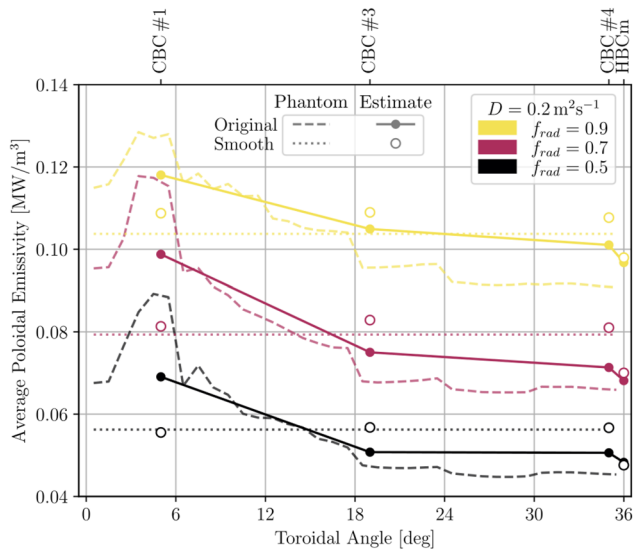


FIG. 14. Predicted response of the final CBCs and HBCm to three different EMC3-EIRENE radiation phantoms (a subset of Fig. 9). The measured chord brightness as a function of the camera toroidal angle (solid line) is compared to the underlying toroidal emissivity profile (dashed line). A reference measurement (circle markers) is performed on a smoothed version of the phantoms, where the toroidal emissivity profile is flattened (dotted line).

underestimate this quantity, while CBC No. 4 overestimates it. The horizontal bolometer camera (HBCm) value in comparison is slightly closer to the local average poloidal emissivity (HBCm, $\varphi = 36^\circ$). In addition, it must be noted that the volume-weighted average of the chord brightness measurements ε_{chord} does not provide an absolutely accurate estimate of the average plasma emissivity. The error between the estimated (ε) and the real plasma emissivity averaged within the camera FoV—which is not addressed here—will in general depend on the specific plasma distribution and LoS geometry.³⁹ A characterization of the error of this method will follow in the future work.

In order to single out any effects that may arise from the mesh choice or the procedure, a second set of three phantoms is investigated. These are a modified version of the same three EMC3-EIRENE emissivity distributions with smoothed toroidal gradients to remove the toroidal asymmetry. For smoothing, it is intended that the emissivity of every individual poloidal slice is rescaled so that the average poloidal emissivity is constant in the toroidal direction. The toroidal emissivity gradient is flattened while keeping the total radiated power value and the poloidal emissivity distribution unchanged. Accordingly, the CBC chord brightness measurements corresponding to these three “smoothed” phantoms show negligible toroidal dependence (see empty circles in Fig. 14). This demonstrates that the optimized CBCs are able to identify the toroidal trends of the averaged poloidal emissivity, despite the low number of bolometer channels. When compared to CBC No. 4, the HBCm response to the smoothed phantoms is considerably lower, which suggests that the HBCm proxy might be intrinsically underestimating the local plasma emissivity.

These findings show the impact of the local emissivity distribution and the viewing geometry on the final P_{rad} output from the camera. Assuming an asymmetric distribution similar to Fig. 9, a single localized radiated power measurement at the W7-X triangular plane ($\varphi = 36^\circ$) will consistently underestimate the total P_{rad} when extrapolated to the full torus. This is because the P_{rad} proxy is based on a quantification of the plasma emissivity averaged within the camera FoV [Eqs. (B4) and (B5)], which is then multiplied by the whole plasma volume [Eq. (B6)]. Conversely, a localized measurement at the bean-shaped plane ($\varphi = 0^\circ$) will overestimate it.

To quantify an overall error associated with our P_{rad} proxy method, we apply it to the HBCm synthetic measurements of the six synthetic cases presented here (three EMC3-EIRENE phantoms + three corresponding “smoothed” versions). We express the deviation of each of the six estimates to the nominal total P_{rad} as a percentage error (negative is underestimation, positive is overestimation). When we calculate the mean value and the standard deviation over this set of six percentage errors, we get a discrepancy $\delta_{HBCm} = (-12.2 \pm 4.6)\%$. As expected, the proxy based on HBCm considerably underestimates the total P_{rad} by more than 10% on average.

Solutions to overcome this inaccuracy might involve employing a wide toroidal view bolometer camera or re-scaling the poloidally averaged local emissivity based on the profile information provided by the CBCs. We find that the most accurate proxy for the total P_{rad} is represented by a simple average of the three CBC emissivity estimates. The simple average is possible since the three considered cameras provide three equally spaced, toroidally localized measurements. Furthermore, all three CBCs cover roughly the

same amount of plasma volume with similar numbers of channels. This yields a fairly uniform toroidal coverage of the stellarator half-module.

When this CBC-averaged P_{rad} proxy is employed, the average percentage error is reduced to $\delta_{CBCs} = (0.7 \pm 2.8)\%$. Not only the intrinsic underestimation is corrected, but also the standard deviation of the method is improved in the averaging process. A further test performed on a large dataset of 50 000 mock-up radiation phantoms yielded similar results in terms of improved accuracy and precision. The larger dataset contained both edge and core radiation phantoms, X-/O-point localized emission, and poloidal as well as toroidal asymmetries.

Four CBCs are proposed in this study, all four within the same half-module. This choice is limited by time and space requirements for diagnostic installation before the next experimental campaign. In the future, including more CBCs will further refine the total P_{rad} proxy and help move toward 3D radiation tomography capability. EMC3-EIRENE modeling (e.g., Fig. 9) and divertor bolometry measurements from the last experimental campaign⁴² suggest that better coverage of the divertor region would be especially beneficial.

Three out of the four CBC prototypes have successfully passed the design, manufacturing, and assembly phases and are currently installed in W7-X. These first CBC prototypes are, namely, CBCs Nos. 2, 3, and 4. CBC No. 1 was initially given a lower priority due to tighter diagnostic port constraints. Without CBC No. 1, the performance of the CBC-average proxy is worsened, causing the average percentage error on the six cases to increase to $\delta_{CBCs} = (-3.7 \pm 6.0)\%$. Investigating an upgrade with the inclusion of CBC No. 1 and other CBC iterations will be the scope of future work.

V. CONCLUSIONS

An analysis of EMC3-EIRENE simulated results in the Wendelstein 7-X (W7-X) standard magnetic field configuration revealed significant variations in the toroidal distribution of the plasma radiated power density. The expected asymmetry amounts to up to $\pm 30\%$ for typical plasma parameters, reducing at higher diffusivities and radiated power fractions. In all investigated conditions, the poloidally averaged plasma emissivity is found to peak in the divertor region. The Compact Bolometer Camera (CBC) design is introduced with the purpose of assessing the toroidal and poloidal asymmetries. The sightline geometry is optimized in terms of the synthetic camera response to a set of radiation phantoms. All the optimized CBCs exhibit sufficient spatial resolution to identify poloidal radiation asymmetries. Additionally, the CBCs are capable of providing a proxy for the local plasma radiated power with $< 5\%$ discrepancy compared to a higher resolution 32-channel reference. A further test confirmed the capability of the CBCs to reconstruct the toroidal trend of the average poloidal plasma emissivity. Including the toroidal profile information from three toroidally separated CBCs results in a significantly improved total radiated power proxy. Three out of the four designed CBC cameras have been installed at W7-X. The first results on their performance are foreseen for the next experimental campaign.

ACKNOWLEDGMENTS

This work has been carried out within the framework of the EUROfusion Consortium, funded by the European Union via the

Euroatom Research and Training Program (Grant Agreement No. 101052200—EUROfusion). Views and opinions expressed are, however, those of the author(s) only and do not necessarily reflect those of the European Union or the European Commission. Neither the European Union nor the European Commission can be held responsible for them. The authors acknowledge M. Marquardt, S. Wollert, K. Höchel, R. Laube, and T. Przykopp for support in DAQ, testing, and assembly.

AUTHOR DECLARATIONS

Conflict of Interest

The authors have no conflicts to disclose.

Author Contributions

G. Partesotti: Conceptualization (equal); Formal analysis (lead); Writing – original draft (lead); Writing – review & editing (lead). **F. Reimold:** Conceptualization (equal); Resources (lead); Supervision (lead); Validation (equal); Writing – review & editing (supporting). **J. Ruhnau:** Conceptualization (equal); Validation (equal). **A. Tsikouras:** Formal analysis (supporting); Validation (supporting). **D. Kubeneck:** Conceptualization (supporting); Formal analysis (supporting). **D. Zhang:** Resources (supporting); Writing – review & editing (supporting). **P. Geißler:** Formal analysis (supporting).

DATA AVAILABILITY

The data that support the findings of this study are available from the corresponding author upon reasonable request.

APPENDIX A: CBC DESIGN

Many aspects of the CBC design can be seen as a simplification of the pre-existing core and divertor bolometry systems,¹² with the aim of reducing engineering cost and required port space. The CBC detectors follow the standard design, which is also implemented in the core and divertor bolometry systems: the absorber element is a C-coated 1.5×4 mm Au foil of $5 \mu\text{m}$ thickness, and the meander is Pt on a silicon nitride Si_3N_4 substrate.^{10,12,14}

To provide protection from the plasma heat load, the detectors are housed inside a plain steel box (central panel of Fig. 4). The box is copper-coated (2 mm) on the inside to more efficiently distribute the impinging heat within the material (inertial cooling concept). An additional aluminum casing blocks infrared radiation from the warm housing to the temperature-sensitive detectors. The detectors are fixed to an aluminum plate that is thermally insulated from the housing via PEEK insulation washers, ensuring a stable operating temperature for the detectors.

A cutout with fitted metallic mesh defines the camera pinhole while shielding the detectors from the high-power microwaves. As in the core bolometry and divertor bolometry systems, the mesh wires have a diameter (thickness) of $90 \mu\text{m}$ and 0.24 mm spacing (microwave transmission factor of 5%, optic throughput of 53%).^{12,43} All the box closure gaps are tight against microwaves, screening the inside of the detector housing from stray radiation. An

outlet piece at the back shields the signal cables and carries the bundle up to the diagnostic port flange in a steel guide tube, as reported in Fig. 5.

Thanks to its lightweight design, the CBC can be directly fastened to the port liner, the dedicated system of cooling pipes that protects the diagnostic port walls in W7-X.²⁵ Mounting on the cooled port liner provides a heatsink to the inertially cooled diagnostic between experiments. The heatsink is optimized by adding a SIGRAFLEX (graphite) interlayer that improves the thermal contact to the camera box steel base plate and provides a better fitting of the strongly shaped port liner cooling pipes. A study on the thermal connection between the port liner cooling pipes and the base plate was carried out to identify the optimal contact geometry and validate the heat transfer.⁴⁴ Although the two materials in contact (pipes and CBC base plate) are both steel, the tests are performed on aluminum parts. Using aluminum ensures smaller temperature gradients (higher conductivity), simplifying the analysis. We assume the thermal contact conductance (which quantifies the imperfect touch between two surfaces) of the steel-SIGRAFLEX contact to be comparable to the one of SIGRAFLEX with an aluminum piece of equivalent geometry. This assumption is possible since the graphite-metal conductance mostly depends on the topology of the two surfaces in contact rather than the material of choice.⁴⁵ In addition, the dominant effect in lab experiments was the reduced conductivity of the SIGRAFLEX and the contact area, not the material selection. What remains to be determined is the thermal conductivity of the SIGRAFLEX layer in the direction perpendicular to its surface and the dependence of the thermal contact on other experimental conditions such as surface pressure and geometry.

A series of lab experiments investigated the thermal contact conductance between different aluminum surfaces and a varying number of 1 mm-thick SIGRAFLEX foils at different applied torques.⁴⁴ The thermal contact conductance across the aluminum-SIGRAFLEX surface was found to increase proportionally to the thickness of the SIGRAFLEX layer. However, a single 1 mm foil was chosen for the design to simplify the installation procedure. The findings show that the 1 mm SIGRAFLEX interlayer improves the thermal contact resistance from $R = 0.35 \text{ kW}^{-1}$ to $R = 0.10 \text{ kW}^{-1}$ for an Al/Al interface, or a 70% reduction of the temperature increase at the same applied power. Increasing the torque applied to clamp the interface material (in the range $5.2\text{--}6 \text{ N m}^{-1}$) seemed to produce a less significant effect on the thermal contact. Torque values above the minimal requirement caused a slight, but visible, bending of the aluminum parts, possibly reducing the contact surface area.⁴⁴

Assuming a maximum expected heat load of 120 kW m^{-2} for 5 min of experiment time, a set of heat transfer simulations was performed for the steel/SIGRAFLEX contact. A conservative value of $k = 2.5 \text{ W m}^{-1} \text{ K}^{-1}$ for the SIGRAFLEX thermal conductivity was applied to simulate the imperfect thermal contact between the two surfaces, estimated from the experiments on the aluminum components.⁴⁶ The simulation results satisfied all the installation requirements, showing functional heat separation between the cover and detectors with only minimal thermal drifts at the detectors. The temperature difference is $\Delta T < 1 \text{ }^\circ\text{C}$, far from the safety limit of $200 \text{ }^\circ\text{C}$ to prevent detector damage.¹¹ In comparison, the typical temperature increase following radiation absorption is a fraction of a degree, while that due to the excitation of the bridge can be significant (a few degrees).⁴⁷ The maximum temperature rise on the CBC

cover for long (5 min) plasma discharges remained well below the recrystallization point of steel ($400\text{--}700 \text{ }^\circ\text{C}$), considered to be the safety level.⁴⁴ In the future, the inertially cooled housing is intended to be replaced with an actively cooled, 3D-printed structure to allow for compatibility with the steady-state operation of W7-X.

The CBC was designed to satisfy the standard requirements of passive diagnostics at W7-X, which are not discussed here. An overview of the design criteria for the resistive bolometer cameras at W7-X can be found in Ref. 12.

APPENDIX B: GEOMETRY MATRIX

Resistive bolometer foils measure the power radiated by the plasma integrated along their LoS. The spatial distribution of the plasma radiated power density—often named emissivity distribution in tomography work—is denoted with $\epsilon(\vec{r})$ (W m^{-3}). Here, r is the 3D coordinate inside the plasma volume. The photon absorption efficiency of common C-coated gold absorbers is effectively close to unity in the relevant range of $1.5 \text{ eV--}25 \text{ keV}$.⁴⁸ Fusion plasmas in current-day devices emit only a negligible amount of energy outside this energy range. Therefore, the wavelength dependence of the plasma emissivity and of the photon absorption coefficient in the absorber medium are usually disregarded. The statistical process of photon absorption can be favored with a thicker absorber,⁴⁸ at the expense of a lower sensitivity and longer cooling time (due to the higher thermal mass).⁴⁷ Due to the high absorption efficiency across the majority of the plasma radiation spectrum in W7-X,¹² here we assume that 100% of the radiation power integrated inside the detector FoV is collected.

Assuming negligible opacity and reflections, the power p_i (W) absorbed by the i th bolometer foil can be calculated through¹⁴

$$p_i = \int \epsilon(\vec{r}) \frac{e_i}{4\pi} ds, \quad (\text{B1})$$

where ds is an element of infinitesimal length along the LoS, and e_i ($\text{m}^2 \text{ sr}$) is the etendue or light acceptance of the optical system (line approximation).¹⁴ The etendue is defined as

$$e = \Omega A_D \cos(\beta), \quad (\text{B2})$$

$$= \frac{A_P \cos(\alpha)}{d^2} A_D \cos(\beta), \quad (\text{B3})$$

when Ω (sr) is the solid angle subtended by the detector to the pinhole, A_D is the detection area of the bolometer foil, and β is the angle subtended from the foil normal vector to \vec{d} , the vector connecting detector and pinhole center points (see Fig. 15). In the explicit expression of the solid angle, A_P is the pinhole surface area, $d = |\vec{d}|$ is the foil-to-pinhole distance, and α is the angle between the foil axis and the pinhole axis.

As shown in Fig. 15, the FoV of each detector can be subdivided into two domains in 3D space: the full region and the shadowed region. Point sources radiating within the full region are observed by the full surface of the foil. Emitters in the shadowed region see the foil only partially, and their contribution to the overall signal is weaker. Direct and shadowed regions make up the entirety of the detection volume.

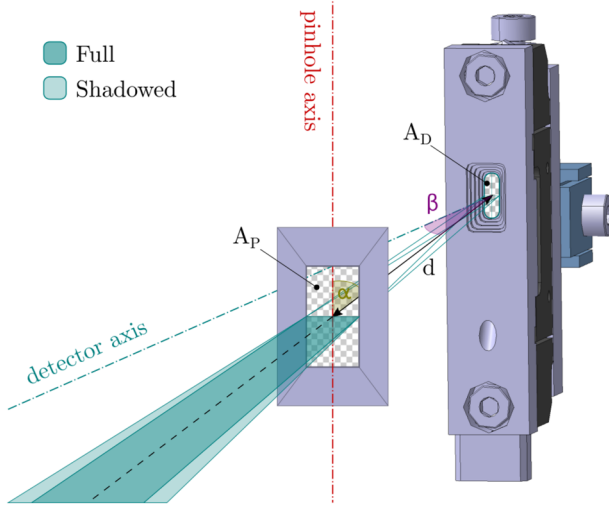


FIG. 15. Simplified model of the detector-pinhole geometry. The normal vectors are indicated with dashed-dotted lines. The detector LoS is indicated with color bands at different shades to visualize the fully covered (direct) and partially covered (shadowed) regions.

If the length d_{LoS} of the LoS inside the plasma volume is known, it is possible to calculate the average emissivity ϵ_{chord} ($W\ m^{-3}$)—or chord brightness—measured within the single LoS using¹⁴

$$\epsilon_{chord, i} = \frac{4\pi}{e_i d_{LoS, i}} P_i. \quad (B4)$$

When multiple active bolometer channels m are available, the individual chord brightness measurements can be combined in a weighted average to estimate the average plasma emissivity $\langle \epsilon \rangle$,¹⁴

$$\langle \epsilon \rangle = \frac{1}{\sum V_{LoS}} \sum_{i=0}^m \epsilon_{chord, i} V_{LoS, i}, \quad (B5)$$

where the weights V_{LoS} are the intersection volume between each LoS and the plasma.

A proxy for the total plasma radiated power can now be extrapolated from this measured average emissivity by multiplying it by the total plasma volume V_{plasma} inside the whole machine (including the SOL),

$$P_{rad} = \langle \epsilon \rangle V_{plasma}. \quad (B6)$$

In standard magnetic field configuration $V_{plasma} \sim 43.5\ m^3$. When modeling the detector response to a given spatial distribution of plasma emissivity, it is convenient to discretize said emission volume using a finite grid of size n with emissivity per voxel values $\epsilon^n = [\epsilon_1, \dots, \epsilon_n] = [\epsilon(\vec{r}_1), \dots, \epsilon(\vec{r}_n)]$. For a given emissivity distribution, each detector signal is solely dependent on the optical characteristics of the viewing geometry. In this case, the integral in Eq. (B1) can be approximated by matrix multiplication. This expression uses the so-called geometry—or transfer—matrix G (m^3). For a set of m detector channels, the geometry matrix takes the shape $m \times n$, and

the measurement $d^m = [p_1, \dots, p_m]$ can be calculated through the linear equation

$$d^m = G^{m \times n} \cdot \epsilon^n + \delta^m, \quad (B7)$$

having defined δ^m the error/uncertainty of the measurement. In particular, in the case of zero-opacity plasma, the power incident on each foil is

$$p_i = \sum_{j=0}^n G_{ij} \epsilon_j + \delta_i. \quad (B8)$$

Here, the element G_{ij} fully describes the contribution of the emission ϵ_j from the j th voxel onto the i th channel and encloses all the necessary information for the forward calculation of bolometry synthetic data. From Eq. (B1), we can then deduce that the geometric factor is equivalent to

$$G_{ij} = \frac{e_i}{4\pi} \langle ds \rangle_{ij}, \quad (B9)$$

when $\langle ds \rangle_{ij}$ is a measure of the coverage of the j th voxel offered by the i th LoS. This measure is related to the average LoS path length within that voxel, which can be quantified via ray tracing.

APPENDIX C: RAY TRACING

In a ray-tracing environment, each detector can be modeled as a two-dimensional target (foil) enclosed within a camera box and viewing the plasma through a rectangular aperture (pinhole). The housing box is here assumed to be composed of a perfectly absorbing material. Using Cherab's dedicated diagnostic package, the geometry matrix can be computed for the W7-X machine geometry, taking into account realistic occlusion effects from the vessel walls.⁴¹ Although reflections can be included as well, they have not been implemented here as their relevance for the bolometry system is negligible (in particular in the C-environment of W7-X).

A three-dimensional geometry matrix is traced for each detector according to the machine coordinates of the bolometer cameras. The coordinates are metrologically calibrated in the vented vessel (1 mm accuracy), but some deviations in geometry can be expected as the plasma vessel deforms during evacuation. So far, these errors are not accounted for in the analysis. Ray tracing is performed on a 72° slice of a regular hollow cylindrical mesh (4.2 m minor radius, 6.4 m major radius, 2.2 m height). The mesh is sectioned with 288 steps in the toroidal direction, 77 steps in the vertical direction z , and 70 steps in the major radius direction R . The resulting voxel size on this ($288 \times 77 \times 70$) mesh amounts to 28.5×28.5 mm in the poloidal plane, and $\Delta\varphi = 0.25^\circ$ spacing in the toroidal direction. The toroidal spacing corresponds to ~ 20 mm at the inboard side up to ~ 28 mm at the outboard side of the cylinder. This resolution is comparable to the average spatial resolution of the core and divertor bolometry systems [Figs. 2(b) and 2(e)] as characterized by the distance between neighboring central LoS axes.¹⁴ Realistic occlusion and cropping of the LoS cones and LoS intersection points are computed by using a triangle mesh of the W7-X machine walls. A total number of 10^7 random rays is traced from each channel, which was found to ensure good statistics for a reasonable computational cost (a few minutes of run-time per detector on a local machine).

The bolometer LoS is traced in three-dimensional space. In tokamaks, however, the assumption of toroidal symmetry is often applied. In this simplified case, emissivity studies and tomographic inversions can be reduced from a 3D problem to a 2D problem in the poloidal plane. Accordingly, the geometry matrix can be collapsed to 2D by summing up all voxel values in the toroidal direction. An example of this geometry matrix collapsed to (R, z) coordinates is reported in Fig. 16(a) for CBC No. 1 [the geometric factor information is the result of ray tracing the LoS geometry schematized in Fig. 4 left-hand side and Fig. 2(a)]. The same toroidal symmetry assumption is, however, not applicable to stellarator machines. At W7-X, a similar approximation is often applied: constant plasma emissivity along the magnetic field lines. This assumption is expected to hold on partially.²⁰ As addressed in Sec. III B, the average poloidal emissivity distribution resulting from EMC3-EIRENE simulations of SOL carbon radiation is not toroidally uniform. This implies that the plasma emissivity within a flux tube is not uniform either. Developing methods aimed at taking into account the asymmetry effect will be the scope of future work.

Applying the assumption of constant ϵ along the field requires interpolating the geometry matrix values from the regular cylindrical mesh to a field-aligned mesh. The latter is here generated starting from one poloidal slice of the cylindrical grid. Figure 17 shows an example when the initial slice of the field-aligned mesh is selected at $\varphi = 36^\circ$. First, the cells belonging to the poloidal slice of the cylindrical grid (gray) are masked using a line contour obtained by extending the LCFS radially outward to include the edge island domain (blue). This contour can be generated from a VMEC equilibrium specific to the magnetic field configuration of interest³⁰ (only the standard magnetic field configuration is taken into consideration in this study). All cylindrical grid cells whose center point falls outside this contour are discarded since they are not part of the plasma volume and often lead to field-line tracing errors. As a result of the masking, we obtain a 2D irregular mesh (red) of $28.5 \times 28.5 \text{ mm}^2$ pixels that partly coincides with the cylindrical mesh. To generate a

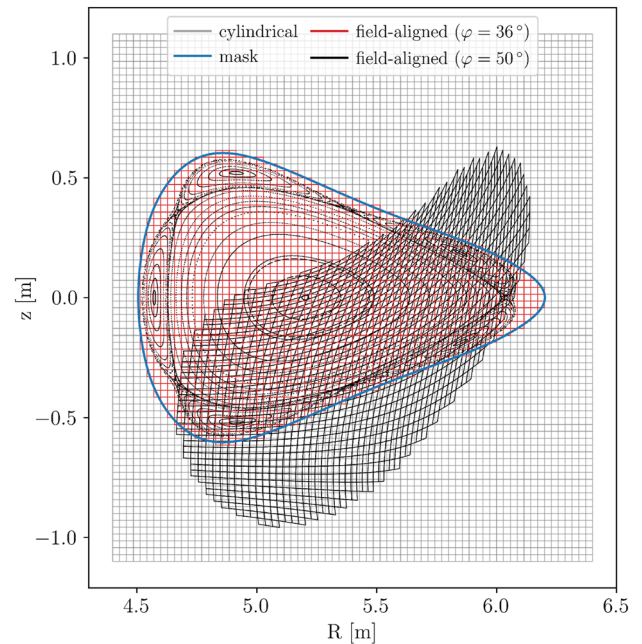


FIG. 17. Grid structure of the field-aligned mesh in the (R, z) poloidal plane. The initial slice (red) is obtained by masking the cylindrical grid (gray) with an extended LCFS (blue). This is then traced along the magnetic field lines to other toroidal angles (black).

3D field-aligned grid, we trace the trajectory of each cell corner point following the magnetic field lines in the backward and forward directions.³⁰ We do this with $\Delta\varphi = 0.25^\circ$ incremental steps until a full magnetic module is covered from $\varphi = 0^\circ$ to $\varphi = 72^\circ$. Due to the tracing, every poloidal cross-section of the final field-aligned grid other than the starting point will present distorted pixel geometry (black) according to magnetic flux conservation.

The interpolation of geometry matrix values from voxels in the regular cylindrical to voxels in the irregular field-aligned mesh is performed with a volume-weighted sum. The geometric factor on each irregular voxel is calculated as a weighted average over the overlapping regular voxels, with the overlap factors counting as weights. Using a volume-overlap weighted sum ensures that the total LoS volume—and, therefore, the geometric factor—is conserved during this step. Finally, the mesh can be condensed by summing up all the magnetically connected voxels in the toroidal direction. Figure 16(b) shows the result of the interpolation procedure applied to the CBC No. 1 geometry matrix.

REFERENCES

- 1 T. S. Pedersen, I. Abramovic, P. Agostinetti, M. A. Torres, S. Äkäslompolo, J. A. Belloso, P. Aleynikov, K. Aleynikova, M. Alhashimi, A. Ali *et al.*, *Nucl. Fusion* **62**, 042022 (2022).
- 2 J. Boscary, G. Ehrke, H. Greuner, P. Junghanns, C. Li, B. Mendelevitch, J. Springer, and R. Stadler, *Fusion Eng. Des.* **166**, 112293 (2021).
- 3 R. A. Pitts, X. Bonnin, F. Escourbiac, H. Frerichs, J. Gunn, T. Hirai, A. Kukushkin, E. Kaveeva, M. Miller, D. Moulton *et al.*, *Nucl. Mater. Energy* **20**, 100696 (2019).

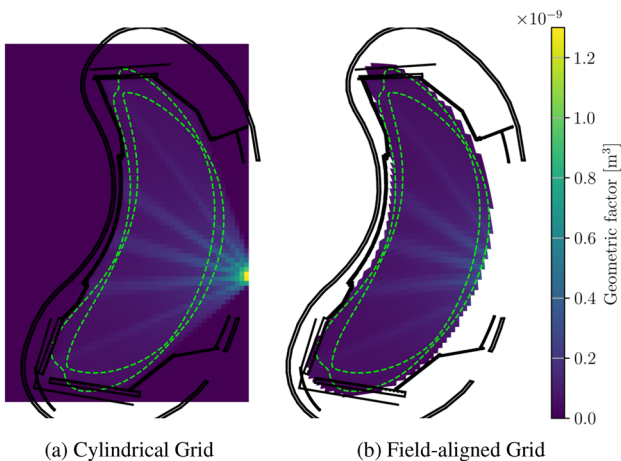


FIG. 16. Collapsed two-dimensional geometry matrix of the CBC No. 1 on (a) the original ray tracing cylinder and (b) interpolated to the field-aligned grid (standard magnetic field configuration). A projected contour of the five magnetic islands contour is visualized with a dashed line.

- ⁴O. Schmitz, Y. Feng, M. Jakubowski, R. König, M. Krychowiak, M. Otte, F. Reimold, T. Barbui, C. Biedermann, S. Bozhnikov *et al.*, *Nucl. Fusion* **61**, 016026 (2020).
- ⁵D. Zhang, R. König, Y. Feng, R. Burhenn, S. Brezinsek, M. Jakubowski, B. Buttenschön, H. Niemann, A. Pavone, M. Krychowiak *et al.*, *Phys. Rev. Lett.* **123**, 025002 (2019).
- ⁶M. Bernert, M. Wischmeier, A. Huber, F. Reimold, B. Lipschultz, C. Lowry, S. Brezinsek, R. Dux, T. Eich, A. Kallenbach, *et al.*, Nuclear materials and energy 12, 111 (2017), part of Special Issue: proceedings of the 22nd International Conference on Plasma Surface Interactions 2016, 22nd PSI.
- ⁷A. Loarte, J. Hughes, M. Reinke, J. Terry, B. LaBombard, D. Brunner, M. Greenwald, B. Lipschultz, Y. Ma, S. Wukitch, and S. Wolfe, *Phys. Plasmas* **18**, 056105 (2011).
- ⁸M. Wischmeier, *J. Nucl. Mater.* **463**, 22 (2015).
- ⁹L. Xiang, F. Militello, D. Moulton, F. Subba, L. Aho-Mantila, D. Coster, M. Wensing, T. Lunt, M. Wischmeier, and H. Reimerdes, *Nucl. Fusion* **61**, 076007 (2021).
- ¹⁰L. Giannone, D. Queen, F. Hellman, and J. Fuchs, *Plasma Phys. Controlled Fusion* **47**, 2123 (2005).
- ¹¹H. Meister, H. Langer, and S. Schmitt, *Fusion Eng. Des.* **112**, 579 (2016).
- ¹²D. Zhang, R. Burhenn, R. Koenig, L. Giannone, P. Grodzki, B. Klein, K. Grosser, J. Baldzuhn, K. Ewert, V. Erckmann *et al.*, *Rev. Sci. Instrum.* **81**, 4 (2010).
- ¹³D. Zhang, H. Thomsen, S. Bozhnikov, T. Bräuer, H. Greve, P. Grodzki, H. Jenzsch, R. König, M. Otte, and T. Pedersen, paper presented at the 40th EPS Conference on Plasma Physics, Espoo, 2013.
- ¹⁴D. Zhang, R. Burhenn, C. D. Beidler, Y. Feng, H. Thomsen, C. Brandt, S. Buller, F. Reimold, P. Hacker, R. Laube *et al.*, *Nucl. Fusion* **61**, 116043 (2021).
- ¹⁵B. J. Peterson, *Rev. Sci. Instrum.* **71**, 3696 (2000).
- ¹⁶Y. Gao, M. W. Jakubowski, P. Drewelow, F. Pisano, A. Puig Sitjes, H. Niemann, A. Ali, B. Cannas *et al.*, *Nucl. Fusion* **59**, 066007 (2019).
- ¹⁷R. Sano, B. J. Peterson, M. Teranishi, N. Iwama, M. Kobayashi, K. Mukai, and S. N. Pandya, *Rev. Sci. Instrum.* **87**, 053502 (2016).
- ¹⁸K. Hammond, Y. Gao, M. Jakubowski, C. Killer, H. Niemann, L. Rudischhauser, A. Ali, T. Andreeva, B. Blackwell, K.-J. Brunner *et al.*, *Plasma Phys. Controlled Fusion* **61**, 125001 (2019).
- ¹⁹D. Kriete, A. Pandey, V. Perseo, J. Schmitt, D. Ennis, D. Gradic, K. Hammond, M. Jakubowski, C. Killer, R. König *et al.*, *Nucl. Fusion* **63**, 026022 (2023).
- ²⁰S. Braun and P. Helander, *J. Phys.: Conf. Ser.* **260**, 012004 (2010).
- ²¹B. J. Peterson, G. Kawamura, P. van de Giessen, K. Mukai, H. Tanaka, R. Sano, S. N. Pandya, S. Dai, S. Masuzaki, T. Akiyama *et al.*, *Nucl. Mater. Energy* **26**, 100848 (2021).
- ²²S. Lazerson, S. Bozhnikov, M. Otte, K. Rahbarnia, M. Jakubowski, Y. Gao, and D. Gates, *Plasma Phys. Controlled Fusion* **60**, 124002 (2018).
- ²³K. Mukai, G. Kawamura, S. Masuzaki, Y. Hayashi, H. Tanaka, B. Peterson, T. Oishi, C. Suzuki, M. Kobayashi, and K. Munechika, *Nucl. Mater. Energy* **33**, 101294 (2022).
- ²⁴Y. Feng, H. Frerichs, M. Kobayashi, A. Bader, F. Effenberg, D. Harting, H. Hoelbe, J. Huang, G. Kawamura, J. Lore *et al.*, *Contrib Plasma Phys.* **54**, 426–431 (2014).
- ²⁵A. Carls, V. Bykov, B. Missal, and L. Wegener, *Fusion Eng. Des.* **146**, 2761 (2019).
- ²⁶T. Andreeva, J. Geiger, A. Dinklage, G. Wurden, H. Thomsen, K. Rahbarnia, J. Schmitt, M. Hirsch, G. Fuchert, C. Nührenberg *et al.*, *Nucl. Fusion* **62**, 026032 (2022).
- ²⁷D. Zhang, R. Burhenn, Y. Feng, R. König, B. Buttenschön, C. Beidler, P. Hacker, F. Reimold, H. Thomsen, R. Laube *et al.*, *Nucl. Fusion* **61**, 126002 (2021).
- ²⁸D. Zhang, B. Buttenschön, S. Jablonski, M. Kubkowska, O. Ford, J. Alcúson, C. Beidler, R. Burhenn, M. Beurskens, A. Langenberg *et al.*, *Plasma Phys. Controlled Fusion* **65**, 105006 (2023).
- ²⁹R. Wolf, A. Ali, A. Alonso, J. Baldzuhn, C. Beidler, M. Beurskens, C. Biedermann, H.-S. Bosch, S. Bozhnikov, R. Brakel *et al.*, *Nucl. Fusion* **57**, 102020 (2017).
- ³⁰M. Grahl, J. Svensson, A. Werner, T. Andreeva, S. Bozhnikov, M. Drevlak, J. Geiger, M. Krychowiak, and Y. Turkin, *IEEE Trans. Plasma Sci.* **46**, 1114 (2018).
- ³¹J. Cosfeld, M. Rack, D. Reiter, P. Drews, Y. Feng, and D. Zhang, *Nucl. Mater. Energy* **18**, 307–311 (2019).
- ³²D. Bold, F. Reimold, H. Niemann, Y. Gao, M. Jakubowski, C. Killer, V. R. Winters *et al.*, *Nucl. Fusion* **62**, 106011 (2022).
- ³³D. Bold, F. Reimold, H. Niemann, Y. Gao, M. Jakubowski, C. Killer, V. R. Winters, N. Maaziz *et al.*, “Impact of spatially varying transport coefficients in EMC3-Eirene simulations of W7-X and assessment of drifts,” [arXiv:2407.12072](https://arxiv.org/abs/2407.12072) [physics.plasm-ph] (2024).
- ³⁴P. Geißler, “Investigating radiation and its distribution in W7X with EMC3/EIRENE,” Technical Report (Max-Planck Institute for Plasma Physics, 2022).
- ³⁵H. Summers, W. Dickson, M. O’mullane, N. R. Badnell, A. Whiteford, D. Brooks, J. Lang, S. Loch, and D. Griffin, *Plasma Phys. Controlled Fusion* **48**, 263 (2006).
- ³⁶Y. Feng, C. Beidler, J. Geiger, P. Helander, H. Hölbe, H. Maassberg, Y. Turkin, D. Reiter *et al.*, *Nucl. Fusion* **56**, 126011 (2016).
- ³⁷Y. Feng, M. Jakubowski, R. König, M. Krychowiak, M. Otte, F. Reimold, D. Reiter, O. Schmitz, D. Zhang, C. Beidler *et al.*, *Nucl. Fusion* **61**, 086012 (2021).
- ³⁸M. Jakubowski, M. Endler, Y. Feng, Y. Gao, C. Killer, R. König, M. Krychowiak, V. Perseo, F. Reimold, O. Schmitz *et al.*, *Nucl. Fusion* **61**, 106003 (2021).
- ³⁹N. Maaziz and F. Reimold, “Improving power balance on Wendelstein 7-X,” in Technical Report No. IPP 2024-10 (Max-Planck Institute for Plasma Physics, 2021).
- ⁴⁰P. L. van de Giessen, G. Kawamura, S. Borling, K. Mukai, and B. J. Peterson, *Rev. Sci. Instrum.* **92**, 033518 (2021).
- ⁴¹C. Giroud, A. Meakins, M. Carr, A. Baciero, and C. Bertrand, CHERAB spectroscopy modelling framework, 2018.
- ⁴²G. Partesotti, F. Reimold, G. A. Wurden, B. J. Peterson, D. Zhang, and K. Mukai, in Proceedings of the 26th PSI Conference, Marseille, France, 2024.
- ⁴³D. Zhang, R. Burhenn, M. Hirsch, H. Laqua, R. König, J. Oosterbeek, J. Baldzuhn, P. Grodzki, K. Ewert, K. Grosser *et al.*, in Proceedings of the 38th EPS Conference on Plasma Physics, Strasbourg, France, 2011.
- ⁴⁴A. Tsikouras, “Heat transfer validation of the thermal interface of the new Compact Bolometer Camera in the W7-X reactor,” in Technical Report No. IPP 2024-13 (Max-Planck Institute for Plasma Physics, 2023).
- ⁴⁵R. Dou, T. Ge, X. Liu, and Z. Wen, *Int. J. Heat Mass Transfer* **94**, 156 (2016).
- ⁴⁶A. S. Sabau, “Review of thermal contact resistance of flexible graphite materials for thermal interfaces in high heat flux applications,” in Technical Report No. ORNL/TM-2022/2564 (Oak Ridge National Laboratory, 2022).
- ⁴⁷D. Zhang, H. Meister, L. Giannone, R. König, R. Burhenn, T. Bergmann, D. Chauvin, P. Devynck, P. Grodzki, K. Höchel *et al.*, in 39th EPS Conference on Plasma Physics 2012, EPS 2012 and the 16th International Congress on Plasma Physics, 2012, Vol. 3.
- ⁴⁸H. Meister, M. Willmeroth, D. Zhang, A. Gottwald, M. Krumrey, and F. Scholze, *Rev. Sci. Instrum.* **84**, 123501 (2013).